PCCP

Accepted Manuscript

ROYAL SOCIETY OF CHEMISTRY

www.rsc.org/pccp

Prediction of Spin Orbital Coupling Effects on Electronic Structure of Two Dimensional van der Waals Heterostructures

Baiqing You[1], Xiaocha Wang[1,*], Wenbo Mi[2]

[1]*Tianjin Key Laboratory of Film Electronic & Communicate Devices, School of Electronics Information Engineering, Tianjin University of Technology, Tianjin 300384, China*

[2]*Tianjin Key Laboratory of Low Dimensional Materials Physics and Preparation Technology, Faculty of Science, Tianjin University, Tianjin 300072, China*

[*]Author to whom all correspondence should be addressed.

E-mail: wangxccn@126.com

ABSTRACT

We report a first-principles study on the electronic structure of the van der Waals (vdW) heterostructures consisting with two dimensional (2D) materials. Herewith, we focus on the effects of spin orbital coupling (SOC) and vdW forces. It is found that all 2D vdW heterostructures can preserve the electronic structure of the isolated 2D materials in the heterostructures. The 2D vdW h-BN/G and h-BN/BP heterostructures show the *n*-type Schottky barriers. The MoS_2/G heterostructures show the *p*-type doping and a strong spin splitting due to SOC, which are the important features that provide a promising future for the application on electronics, optoelectronics and spin-filter devices.

Keywords: Two dimensional semiconductors; van der Waals; Heterostructures; Spin orbital coupling

INTRODUCTION

Since the adoption of mechanical exfoliation method to obtain graphene (G) in graphite, graphene has been extensively studied due to its remarkable electrical and mechanical properties, such as the high carrier mobility and high thermal conductivity.[1] However, graphene is a zero band gap semiconductor, where the lack of controlled way to introduce a band gap limits its applications.[2-3] Thus, other 2D ultrathin vdW materials attracted much attention,[4] such as black phosphorus (BP), hexagonal boron nitride (h-BN), molybdenum disulphide (MoS_2) and transition-metal dichalcogenides.[3,5] By incorporating the 2D ultrathin vdW materials, the heterostructures have been widely studied in theory and experiments, and their overall properties exceed its individual parts.[6] In recent years, black phosphorus has become a hot topic, where its bulk is the most stable phosphorus allotrope at room temperature.[7] Similar to graphene, BP also has a honeycomb lattice, but it is not planar.[8] The monolayer BP is a direct band gap semiconductor with a predicted band gap of 2.0 eV that can be combined into the field effect transistor.[6,8] BP exhibits some remarkable electronic properties superior to graphene, such as a high hole mobility and a very high leakage current modulation rate (which is 10^4 times than graphene) that is similar to the traditional materials in silicon electronic circuits.[6,9] h-BN is a 2D sp^2-hybridized, commonly known as white graphene. Its composition is arranged in honeycomb

alternating boron and nitrogen atoms, so the h-BN powder is traditionally used as lubricant.[10] Monolayer h-BN is a direct band gap semiconductor and multilayer is an indirect band gap semiconductor. The experimental band gap of bulk h-BN is 5.97 eV,[10] so it is a wide band gap semiconductor.[11] Owing to its high-k dielectric properties, h-BN has been used as a charge leakage barrier in the electronic devices.[2,10] MoS_2 is one of the stable layered transition metal dichalcogenide, which has a hexagonal structure that is similar with grapheme.[12] The band gap turns from indirect band of 1.2 eV in bulk to direct gap of 1.9 eV in monolayer MoS_2.[13] Since monolayer MoS_2 has a band gap, it can be used in field effect transistor. Compared with graphene, MoS_2 has a high switching rate, but a lower electron mobility.[14]

Currently, the 2D vdW heterostructures are considered to be a novel way to build a new device and play an important role in the high-speed electronic and optoelectronic devices.[2,15] Experimentally, Gong *et al.* achieved in the vertical stacked bilayers and in-plane interconnected WS_2/MoS_2 heterostructures, which opens up the possibility to create unprecedented architectures using 2D vdW materials.[15] A buried metal-gate field-effect transistor using a stacked h-BN and chemically vapor deposited G heterostructure is demonstrated.[16] Shi *et al.* reported the van der Waals epitaxy of MoS_2 layers using G as growth templates, the synthesized two-dimensional MoS_2/G hybrids possess great potential toward the development of new optical and electronic devices as well as a wide variety of newly synthesizable compounds for catalysts.[17] Due to the

lack of dangling bonds, the different 2D materials stacked together, both produce new features while maintaining their unique properties.[2] Lee *et al.* report the characterization of the electronic and optoelectronic properties of atomically thin *p-n* heterojunctions fabricated by van der Waals assembly of transition-metal dichalcogenides.[18] Recently, a band split of surface state due to SOC has attracted considerable attentions.[19,20] The Rashba spin-orbit coupling and Dresselhaus spin-orbit coupling that exist in two dimensional electron gas also exist in the semiconductor heterostructures.[21] SOC is the main factor of the topological insulator.[19] Meanwhile, the giant spin-orbit-induced spin splitting in 2D transition-metal dichalcogenide semiconductors has been reported,[22-25] which has great potential applications in optoelectroncs and spin-dependent valleytronics devices.[26-27] However, the SOC effects are not considered in 2D vdW heterostructures.

In this work, we calculated the electronic structures of h-BN/G, MoS_2/G and h-BN/BP vdW heterostructures by considering the spin-orbit coupling. By comparing the three groups of 2D vdW heterostructures, we show that these 2D vdW heterostructures provide a promising future in the electronics, optoelectronics and spin-filter devices.

CALCULATION DETAILS AND MODEL

Our first principles calculations are based on density-functional theory (DFT) and the projector augmented wave method as implemented in the Vienna Ab initio Simulation Package code.[28-30] Exchange and correlation function is used by the Perdew-Burke-Ernzerhof flavor of the spin-polarized generalized gradient approximation (GGA).[31] It is found that the optimized lattice constant of graphene, MoS_2, h-BN, BP calculated by GGA is 2.47 Å, 3.17 Å, 2.51 Å, a=4.24 Å/b=3.24 Å, respectively, which is well consistent with the experimental value of G, MoS_2, h-BN, BP is 2.46 Å, 3.16 Å, 2.50 Å, a=4.24 Å/b=3.24 Å. The electronic band structure of isolated G and monolayer MoS_2 are also well consistent with the experimental results. Meanwhile, the electronic band structure of isolated G and monolayer MoS_2 calculated by GGA are good agreement with experiment.[2] Herewith, we study the heterostructures composed with other 2D materials adhered graphene and MoS_2 by comparing with the isolated graphene and MoS_2. So, the GGA is reasonable. All of the geometry structures are fully relaxed until the total energy and the force on each atom are converged to 10^{-5} eV and 0.01eV/Å, respectively. The plane-wave basis set is converged using a 500-eV energy cutoff. The Brillouin zone is sampled with 6×6×1 k meshes for h-BN/G, MoS_2/G and h-BN/BP 2D vdW heterostructures. A thick vacuum layer of 15 Å is included to ensure decoupling between adjacent slabs. In our theoretical calculations on 2D vdW heterostructures, we employed a semi-empirical DFT-D2 method, which is widely used and has been demonstrated to good description

of long-range weak vdW interactions in molecular surface adsorption and layered structure systems.[2,6] Although we used the spin-polarized calculation, the results indicate that all of the models do not show magnetic moments.

For bulk graphite, h-BN and MoS_2, the space group is P6/MMM, P63/MMC and P63/MMC, respectively. The calculated lattice constants of G, h-BN and MoS_2 monolayer is 2.46 Å, 2.51 Å, and 3.17 Å, respectively. Bulk BP has a rhombic structure with the lattice constants of a=3.24 Å, b=10.19 Å, c=4.24 Å, respectively. The calculated x-y plane lattice constants of bulk BP is a=4.24 Å, b=3.24 Å, respectively. In order to simulate the hybrid 2D vdW heterostructures, we choose two different lattice structures and lattice constants, which make them have a minimal lattice mismatch for each other. Hybid MoS_2/G heterostructures by combining a supercell (4×4) of graphene (001) and a 3×3 supercell of MoS_2 (001), which leads to a small lattice mismatch of 3.44%. Hybid h-BN/G heterostructures by combining a primitive cell (1×1) of graphene (001) and a 1×1 primitive cell of h-BN (001), which leads to a small lattice mismatch of 2%. Hybid h-BN/BP heterostructures by combining an orthogonal supercell ($5\times3\sqrt{3}$) of h-BN (001) and a 3×4 supercell of BP (010), where a and b have a small lattice mismatch of 1.35% and 0.69%, respectively. All of the models are shown in Fig. 1.

In order to discuss the relative stabilities of the 2D vdW heterostructures, the binding energy is calculated, which is defined as $E_b = E_X + E_Y - E_{X/Y}$, where $E_{X(Y)}$

represents the energy heterostructures of $X(Y)$ layer atoms removed, $E_{X/Y}$ is the total energy of the 2D vdW heterostructures, X/Y represents the h-BN/G, MoS_2/G and h-BN/BP, respectively. In order to clarify the nature of charge transfer in the h-BN/G, MoS_2/G and h-BN/BP heterostructures, respectively. We calculate the charge density difference $\Delta\rho$, which is defined as $\Delta\rho=\rho_{X/Y}-\rho_X-\rho_Y$, where $\rho_{X/Y}$, ρ_X and ρ_Y are charge densities of the X/Y, X and Y, respectively.

RESULTS AND DISSCUSION

The binding energy E_b, optimized lattice constants and bond angles of the 2D vdW heterostructures are given in Table 1. The relationship between the binding energy of the three types of heterostructures are model a<c<d<b<e, which indicates that the most stable case is model e. The h-BN/BP 2D vdW heterostructures has the maximum binding energy. The optimized bond angles show little distortions in the three types of 2D vdW heterostructures.

In Fig. 2(a), we illustrate the electronic band structures of the single layer G (1×1). It is clearly seen from Fig. 2(a) that G is a zero band gap and presents linear dispersion relation near Dirac points, which is consistent with the previous theoretical results.[32] Fig. 2(b) shows the electronic band structures of the single layer h-BN (1×1). It is clear that h-BN is a direct band gap semiconductor with a calculated band gap of 4.67 eV.

Actually, h-BN is a wide band gap semiconductor with a experimental band gap of 5.97 eV.[10] The calculated band gap is underestimated by about 22% in GGA, which is in well agreement with the results reported by Giovannetti *et al*.[33] In Fig. 2(c), the band gap of h-BN/G heterostructures is opened at K point of Brillouin zone, showing a band gap of 67.8 meV. Under 1% uniaxial tensile strain, Ni *et al*. predicted a band gap opening of ~300 meV for graphene,[34] which is larger than our calculated value in the heterostructure. Meanwhile, the electronic band characteristics of the monolayer G and h-BN are preserved. Since Fermi level lies in the middle of band gap and the conduction band of h-BN is closer to Fermi level, a *n*-type Schottky barrier ($\Phi_{B,n}$) forms between G and h-BN. An *n*-type Schottky barrier height is defined as $\Phi_{B,n}=E_C-E_F$,[6] where E_C is the conduction band minimum (CBM),[35] and E_F represents Fermi level.[2] Likewise, a *p*-type Schottky barrier heights is $\Phi_{B,p}=E_F-E_V$, where E_V is the valence band maximum (VBM).[6,35] In Fig. 2(c), a small *n*-type Schottky barrier height of $\Phi_{B,n}$=32.7 meV appears. Fig. 2(d) shows the electronic band structure of h-BN/G heterostructure by considering SOC. By comparing Figs. 2(c) and 2(d), one can find that at G point two band gaps of 13.2 and 10.0 meV are induced for σ orbit by SOC, leading to a spin splitting. In Fig. 2(d), at K point, the band moves up 0.1 meV induced by SOC for π orbit, but the band gap does not change. Yao *et al.* reported that the spin-orbit coupling in graphene is taken into account for a opened band gap of 10^{-3} meV and find that the band gap induced by SOC for σ orbit is 9.0 meV at G point,[21]

which is smaller than our results.

Fig. 3 shows the electronic band structures of a 4×4 monolayer G, a 3×3 monolayer MoS_2 and MoS_2/G heterostructures. In Fig. 3(b), one can observe that the monolayer MoS_2 is a direct band gap semiconductor with a band gap of 1.67 eV. In Figs. 3(c), 3(e) and 3(g), the band gaps of MoS_2/1-layer G, MoS_2/2-layer G and MoS_2/3-layer G heterostructures without SOC are opened, which are 4.9 meV, 8.5 meV and 18.6 meV, respectively. It also indicates that the band characteristics of the monolayer G and MoS_2 are preserved. Furthermore, in Fig. 3(c), Fermi level is located at 129.8 meV above VBM and 134.7 meV below CBM of the MoS_2/1-layer G heterostructure, indicating that the band gap is 4.9 meV and it is a *p*-type doping. Li *et al*. reported that different models of graphene/MoS_2 superlattice have a band gap of 0.7 and 1.1 meV, respectively. It is also a *p*-type doping.[13] Our calculated band gap is larger than the results reported by Li *et al*,[13] which can be attributed to the facts that the structure in Ref [12] is MoS_2/G/MoS_2/G superlattice, but in our calculations the structure is an interface. Fig. 3(d) shows the electronic band structure of MoS_2/1-layer G heterostructure by considering SOC. By comparing the electronic band structures in Figs. 3(c) and 3(d), it is found that the band moves up by 12.7 meV and the band gap is reduced to 4.2 meV at K point due to SOC. Figs. 3(e) and 3(g) show the electronic band structure of MoS_2/2-layer G and MoS_2/3-layer G heterostructures without SOC, respectively. Figs. 3(f) and 3(h) give the electronic band structure of MoS_2/2-layer G

and MoS_2/3-layer G heterostructures with SOC, respectively. By comparing Fig. 3(e) with Fig. 3(f), it is also found that the band moves up by 11.1 meV and the band gap reduces to 4.3 meV induced by SOC at K point. By comparing Fig. 3(g) with Fig. 3(h), the band moves up by 18.6 meV and the band gap reduces to 15.1 meV induced by SOC at K point. Therefore, we find that the electronic band upward movement and the band gap reduction with the increase of the number of graphene layers. In Figs. 3(d), 3(f) and 3(h), it is clearly seen that many parts of energy bands split into two energy bands, so a strong spin splitting appears. Particularly, one can find a band splitting at the conduction band edges near K point of Brillouin zone. In Figs. 3(d), 3(f) and 3(h), we find that the conduction band splitting is 0.6, 0.5 and 0.3 meV, respectively. The size of the conduction band splitting decreases with the increase of the number of graphene layers. The spin-splitting of MoS_2 in the heterostructures is the same as that of the isolated monolayer MoS_2. The SOC-induced band splitting is substantial due to the presence of the *d* orbitals of the heavy metal Mo atoms.

Fig. 4 shows the electronic band structure of a $5\times3\sqrt{3}$ supercell of monolayer h-BN, a 3×4 supercell of monolayer BP, and h-BN/BP heterostructure with and without SOC. In Fig. 4(b), it is clear that the monolayer BP is a direct band gap semiconductor with a gap of 0.9 eV. Figs. 4(c) and 4(d) show the electronic band structure of h-BN/BP heterostructures without and with SOC, respectively. In Fig. 4(c), the band gap of h-BN/BP heterostructure without SOC is 0.38 eV, which is consistent with the reported

band gap of 0.35 eV by Cai *et al*.[37] It is found that the states near Fermi level are mainly from BP, and the band gap from the monolayer BP decreased to 0.38 eV. In Fig. 4(d), the band drops 15.2 meV by comparing with the case without SOC. The band gap is increased to 0.40 eV at K point due to SOC. Fermi level locates between the conduction and valence bands and is closer to CBM, where the *n*-type Schottky barrier height ($\Phi_{B,n}$) is 0.17 eV. However, no obvious spin splitting appears. The semiconducting characters of monolayer h-BN and BP are preserved.

Fig. 5 shows the total density of states (TDOS) and partial density of states (PDOS) of the 2D vdW heterostructures. All of the results show that the spin-up and spin-down states are completely symmetrical. In Fig. 5(a), it is clear that the h-BN/G heterostructure is a semiconductor because Fermi level locates between VBM and CBM. Meanwhile, VBM comes from B 2p, N 2p and C 2p states and CBM also comes from B 2p, N 2p and C 2p states. Figs. 5(b), 5(c) and 5(d) show the TDOS and PDOS of MoS_2/1-layer G, MoS_2/2-layer G and MoS_2/3-layer G heterostructures, respectively. In Figs. 5(b), 5(c) and 5(d), all of the results indicate that it is *p*-type doping. A metallic characteristic appears because VBM exits at Fermi level, which suggests that it can be weakly conductive. The VBM comes from C 2p, S 2p and Mo 3d states and the CBM also comes from C 2p, S 2p and Mo 3d states. Fig. 5(d) shows the TDOS and PDOS of h-BN/BP heterostructure. In Fig. 5(d), the results illustrate a semiconducting characteristic because Fermi level locates between VBM and CBM. The VBM comes

from B 2p, N 2p and P 2p states and the CBM also comes from B 2p, N 2p and P 2p states.

In order to further explore the charge transfer in the 2D vdW heterostructures, the isosurfaces of charge accumulation and depletion of 2D vdW heterostructures are shown in Fig. 6. In Fig. 6(a), no significant accumulation of charge between G and h-BN layer appears. In Figs. 6(b)-(d), it is clear that the charge transfers from G to the intermediate region and small amount of charge accumulation between the G and MoS_2 layers, which indicate that the small amount of charge transfer results in the interfacial bonding between G and MoS_2 that takes on weak ionic interactions. Therefore, we observed the *p*-type doping of G on MoS_2 due to the electron transfer from G to MoS_2, as shown in Figs. 6(b)-(d). Moreover, in Fig. 6(e), we observed the significant charge accumulation that is more than that in Figs. 6(b)-(d), resulting in a much stronger ionic interactions.

CONCLUSION

In this work, the main findings of our first-principles DFT calculations on the structural and electronic properties of 2D vdW heterostructures are summarized as follows: For case a-d: (1) the linear electronic bands around Dirac point are preserved; (2) a small band gap opened up at K point. Interestingly, we find that a *n*-type Schottky

barrier heights ($\Phi_{B,n}$) forms between the semi-metallic G and semiconducting h-BN, where the *n*-type Schottky barrier height of $\Phi_{B,n}$ is 32.7 meV; (3) the MoS_2/G heterostructures show the p-doping. By considering SOC, a strong spin splitting appears; (4) a small amount of charge transfer between the layers; (5) for case e, we also find that the semiconducting nature of monolayer h-BN and BP is preserved. Furthermore, a *n*-type Schottky barrier height ($\Phi_{B,n}$) of 0.17 eV appears, but there is no obvious spin splitting phenomenon with SOC; (6) we observed the significant charge accumulation between layers. Therefore, MoS_2/G 2D vdW heterostructures are potential in the spin-filter devices. In addition, the h-BN/G and h-BN/BP 2D vdW heterostructures can be applied into the high performance *p*-type field effect transistor and optoelectronic devices.

ACKNOWLEDGEMENTS

This work was supported by the Key Project of the Natural Science Foundation of Tianjin City (14JCZDJC37800)

REFERENCES

1 H. Y. Guo, N. Lu, J. Dai, X. J. Wu, X. C. Zeng, *J. Phys. Chem. C* 2014, **118**, 14051-14059.

2 J. E. Padilha, A. Fazzio, A. J. R. da Silva, *Phys. Rev. Lett.* 2015, **114**, 066803.

3 G. H. Lee, C. H. Lee, A. M. van der Zande, *APL. Mater.* 2014, **2**, 092511.

4 C. H. Lee, G. H. Lee, A. M. van der Zande, *Nat. Nanotech.* 2015, **150**, 676-681.

5 Y. L. Yuan, X. P. Gong, H. M. Wang, *Phys. Chem. Chem. Phys*. 2015, **17**, 11375-11381.

6 W. Hu, J. L. Yang, *Mater. Sci.* 2015, **06**, 033.

7 H. Liu, A. T. Neal, Z. Zhu, D. Tomanek, X. F. Xu, *ACS Nano.* 2014, **8**, 4033-4041.

8 A. Jain, A. J. H. McGaughey, *Sci. Rep.* 2015, **5**, 8051.

9 L. K. Li, Y. J. Yu, G. J. Ye, Q. Q. Ge, X. D. Ou, H. Wu, D. L. Feng, X. H. Chen, Y. B. Zhang, *Nat. Nanotech.* 2014, **9**, 372-377.

10 M. S. Xu, T. Liang, M. Shi, H. Z. Chen, *Chem. Rev.* 2013, **113**, 3766-3798.

11 X. Lei, X. X. Liang, G. J. Zhao, T. L. Song, *J. Phys.: Conf. Ser.* 2014, **490**, 012171.

12 M. Y. Yin, X. C. Wang, W. B. Mi, B. H. Yang, *Comput. Mater. Sci.* 2015, **99**, 326-335.

13 X. D. Li, S. Yu, S. Q. Wu, Y. H. Wen, S. Zhou, Z. Z. Zhu, *J. Phys. Chem. C* 2013, **117**, 15347-15353.

14 N. Feng, W. B. Mi, Y. C. Cheng, Z. B. Guo, U. Schwingenschlögl, *ACS Appl. Mater. Interfaces.* 2014, **6**, 4587-4594.

15 Y. J. Gong, J. H. Lin, X. L. Wang, *Nat. Mater.* 2014, **13**, 1135-1142.

16 N. Jaina, T. Bansala, C. A. Durcana, Y. Xub, B. Yua, *Elsevier, Carbon.* 2013, **54**, 396-402.

17 Y. M. Shi, W. Zhou, A.Y. Lu, W. J. Fang, Y. H. Lee, *Nano. Lett.* 2012, **12**, 2784-2791.

18 C. H. Lee, G. H. Lee, A. M. van der Zande, W. H. Chen, Y. L. Li, *Nat. Nanotech.* 2014, **9**, 676-681.

19 Y. M. Koroteev, G. Bihlmayer, J. E. Gayone, E. V. Chulkov, *Phys. Rev. Lett.* 2014, **93**, 046403.

20 S. H. Chen, C. R. Chang, *Phys. Rev. B* 2008, **77**, 045324.

21 Y. G. Yao, F. Ye, X. L. Qi, S. C. Zhang, Z. Fang, *Phys. Rev. B* 2007, **75**, 041401.

22 Z. Y. Zhu, Y. C. Cheng, U. Schwingenschlogl, *Phys. Rev. B* 2011, **84**, 153402.

23 D. MacNeill, C. Heikes, K. Mak, Z. Anderson, A. Kormányos, V. Zólyomi, J. Park, D. Ralph, *Phys. Rev. Lett.* 2015, 114, 037401.

24 D. Xiao, G. B. Liu, W. Feng, X. Xu, W. Yao, *Phys. Rev. Lett.* 2012, **108**, 196802.

25 K. F. Mak, K. He, J. Shan, T. F. Heinz, *Nat. Nanotechnol.* 2012, **7**, 494.

26 M. Eginligil1, B. Cao, Z. Wang, X. Shen, C. Cong, J. Shang, C. Soci, T. Yu, *Nat. Commun*. 2015, **6**, 7636.

27 H. Zeng, J. Dai, W. Yao, D. Xiao, X. Cui, *Nat. Nanotechnol.* 2012, **7**, 490.

28 W. Kohn, L. J. Sham, *Phys. Rev.* 1965, **140**, A1133-A1138.

29 P. E. Blöchl, *Phys. Rev. B* 1994, **50**, 17953-17979.

30 G. Kresse, J. Furthmüller, *Phys. Rev. B* 1996, **54**, 11169-11186.

31 J. P. Perdew, K. Burke, M. Ernzerhof, *Phys. Rev. Lett.* 1996, **77**, 3865-3868.

32 N. O. Weiss, H. L. Zhou, L. Liao, Y. Liu, S. Jiang, Y. Huang, X. F. Duan, *Adv. Mater.* 2012, **24**, 5782-5825.

33 G. Giovannetti, P. A. Khomyakov, G. Brocks, P. J. Kelly, van den Brink, J. *Phys. Rev. B* 2007, **76**, 073103.

34 Z. H. Ni, T. Yu, Y. H. Lu, Y. Y. Wang, Y. P. Feng, Z. X. Shen, *ACS Nano.* 2008, **2**, 2301-2305.

35 A. Walsh, J. L. F. Da Silva, S. H. Wei, C. Körber, A. Klein, L. F. J. Piper, A. DeMasi, K. E. Smith, G. Panaccione, P. Torelli, D. J. Payne, A. Bourlange, R. G. N. Egdell, *Phys. Rev. Lett.* 2008, **100**, 167402.

36 Y. Q. Cai, G. Zhang, Y. W. Zhang, *J. Phys. Chem. C* 2015, **119**, 13929-13936.

FIGURE CAPTIONS

Fig. 1. Top- and side-view models of heterostructures, (a) h-BN/G, (b) MoS_2/1-layer G, (c) MoS_2/2-layer G, (d) MoS_2/3-layer G, (e) h-BN/BP.

Fig. 2. Electronic band structure of a 1×1 primitive cell of (a) monolayer G and (b) monolayer h-BN, (c) h-BN/G heterostructure without SOC. The gray and red color indicates G and h-BN, respectively. (d) h-BN/G heterostructure with SOC. The Fermi level is set to 0 eV on the energy axis.

Fig. 3. Electronic band structure of (a) a 4×4 supercell of monolayer G and (b) a 3×3 supercell of monolayer MoS_2. (c), (e) and (g) are the electronic band structure of MoS_2/1-layer G, MoS_2/2-layer G and MoS_2/3-layer G heterostructures without SOC, respectively. The gray and red color indicates G and MoS_2, respectively. (d), (f) and (h) are the electronic band structure of MoS_2/1-layer G, MoS_2/2-layer G and MoS_2/3-layer G heterostructures with SOC, respectively. The Fermi level is set to 0 eV on the energy axis.

Fig. 4. Electronic band structure of (a) a $5\times3\sqrt{3}$ supercell of monolayer h-BN, (b) a

3×4 supercell of monolayer BP, (c) h-BN/BP heterostructures without SOC. The gray and red color indicates h-BN and BP, respectively, (d) h-BN/BP heterostructures with SOC. The Fermi level is set to 0 eV on the energy axis.

Fig. 5. The total density of states (TDOS) and partial density of states (PDOS) of (a) h-BN/G, (b) MoS_2/1-layer G, (c) MoS_2/2-layer G, (d) MoS_2/3-layer G and h-BN/BP 2D vdW heterostructures without SOC.

Fig. 6. The charge density difference (a) h-BN/G (0.01 e/Å^3), (b) MoS_2/1-layer G (0.01 e/Å^3), (c) MoS_2/2-layer G (0.01 e/Å^3), (d) MoS_2/3-layer G (0.01 e/Å^3), (e) h-BN/BP (0.0025 e/Å^3). The red and blue regions represent electron increase and decrease, respectively.

TABLE NOTES

model	case	E_b	a(Å)	b(Å)	c(Å)	α(deg)	β(deg)	γ(deg)
h-BN/G	(a)	0.340	2.488	2.488	16.741	90.000	90.000	120.00
MoS_2/1-layer G	(b)	7.720	9.785	9.785	20.544	90.000	90.000	120.00
MoS_2/2-layer G	(c)	6.040	9.815	9.815	23.805	90.000	90.000	120.00
MoS_2/3-layer G	(d)	6.080	9.828	9.828	27.206	90.000	90.000	120.00
h-BN/BP	(e)	11.44	12.644	13.153	20.053	90.001	89.998	90.000

TABLE 1. Binding energy E_b (eV) and optimized lattice constants and bond angles

Fig. 1. Baiqing You *et al.*

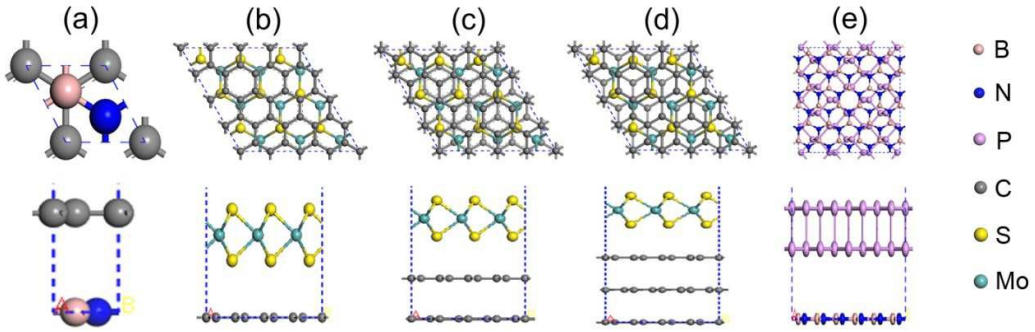

Fig. 2. Baiqing You *et al.*

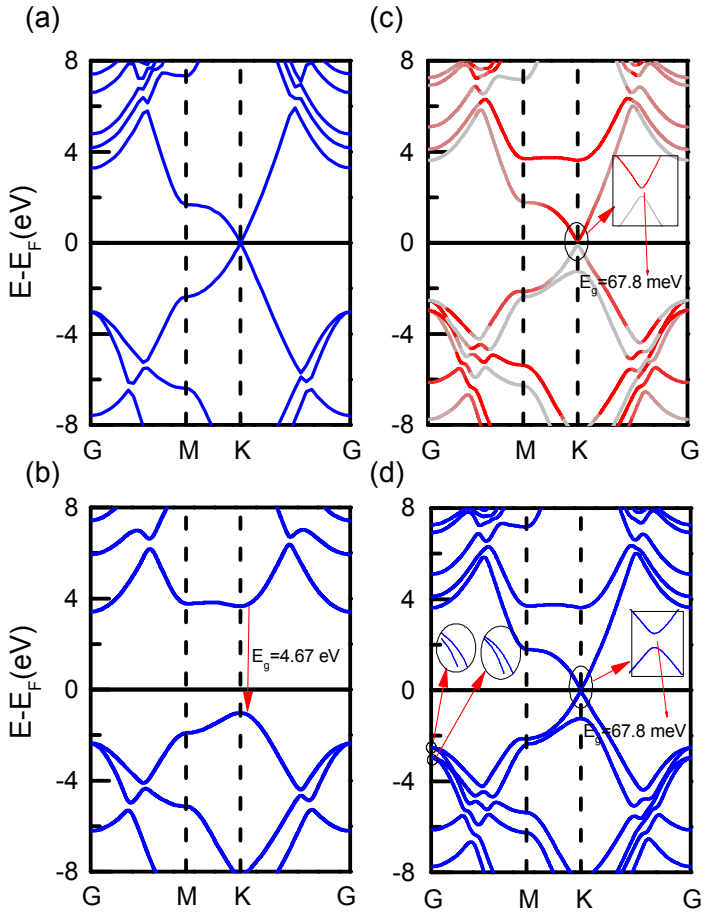

Fig. 3. Baiqing You *et al.*

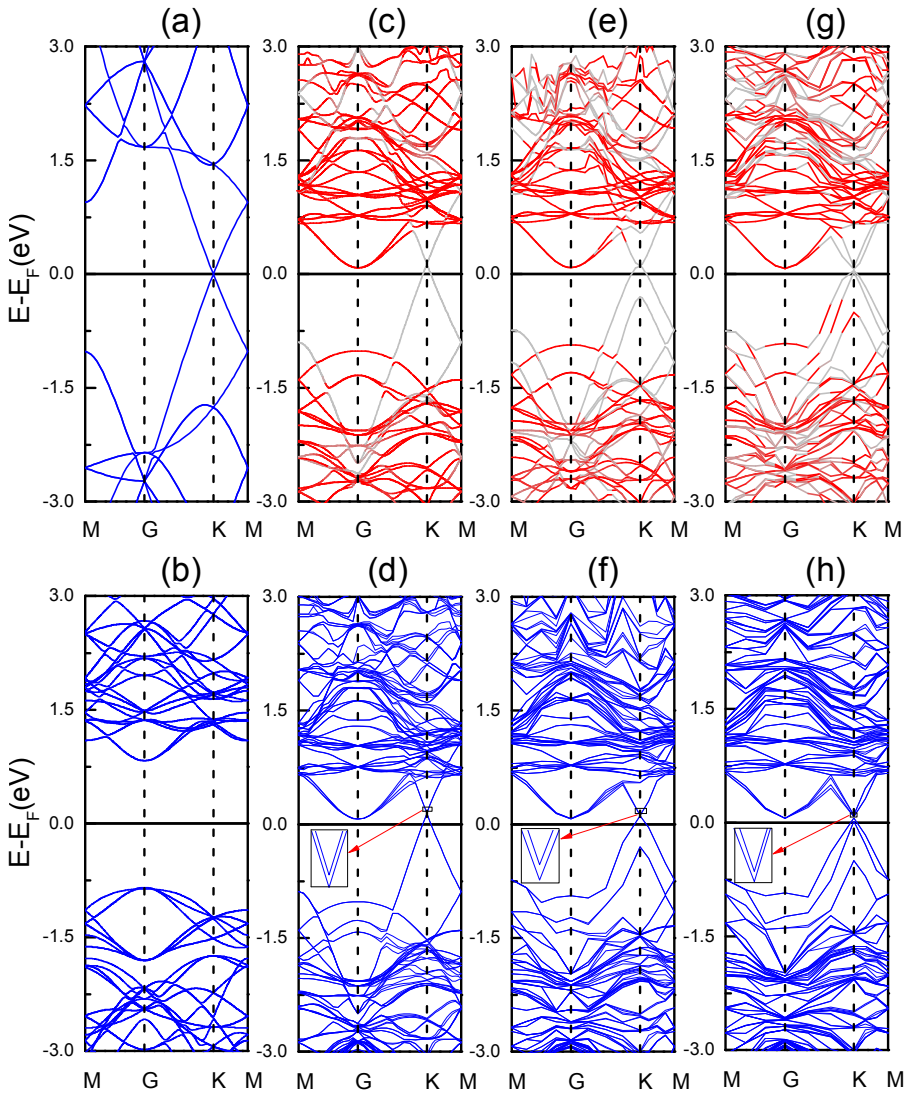

Fig. 4. Baiqing You *et al.*

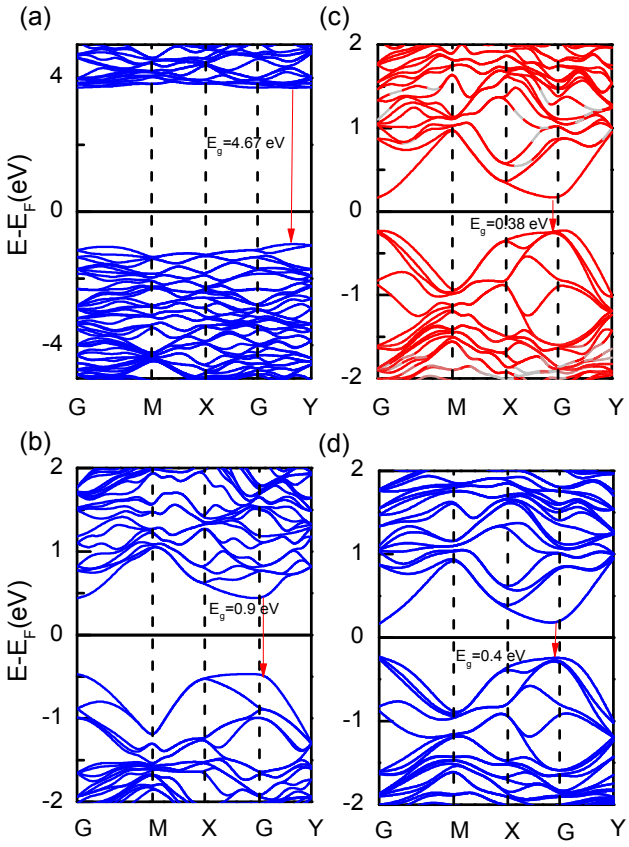

Fig. 5. Baiqing You *et al.*

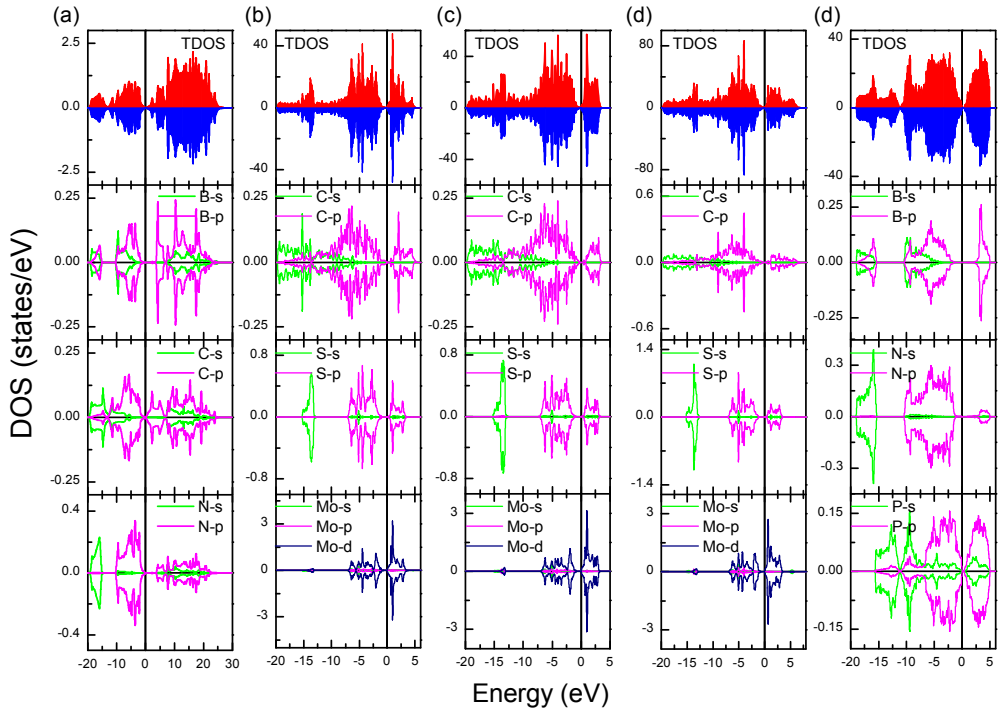

Fig. 6. Baiqing You *et al.*